



1 **Revisiting the trend in the occurrences of the “warm Arctic-cold Eurasian continent”**
2 **temperature pattern**
3 Lejiang Yu^{1,2*}, Shiyuan Zhong³, Cuijuan Sui⁴, and Bo Sun¹
4 1MNR Key Laboratory for Polar Science, Polar Research Institute of China, Shanghai, China
5 2 Southern Marine Science and Engineering Guangdong Laboratory (Zhuhai), Zhuhai, Guangdong,
6 China
7 3Department of Geography, Environment and Spatial Sciences, Michigan State University, East
8 Lansing, MI, USA
9 4 National Marine Environmental Forecasting Center, Beijing, China
10
11 *Corresponding Author's address
12 Dr. Lejiang Yu
13 MNR Key Laboratory for Polar Science, Polar Research Institute of China
14 451 Jinqiao Rd. Shanghai, 200136
15 Phone: 86-21-58712034,
16 Email: yulejiang@sina.com.cn
17
18
19
20
21
22



23 **Abstract.** The recent increasing trend of “warm Arctic, cold continents” has attracted much attention,
24 but it remains debatable as to what forces are behind this phenomenon. Here, we revisited
25 surface-temperature variability over the Arctic and Eurasian continent by applying the
26 Self-Organizing-Map (SOM) technique to gridded daily surface temperature data. Nearly 40% of the
27 surface temperature trends are explained by the nine SOM patterns that depict the switch to the current
28 warm Arctic-cold Eurasia pattern at the beginning of this century from the reversed pattern that
29 dominated the 1980s and the 90s. Further, no cause-effect relationship is found between the Arctic
30 sea-ice loss and the cold spells in high-mid latitude Eurasian continent suggested by earlier studies.
31 Instead, the increasing trend in warm Arctic-cold Eurasia pattern appears to be related to the anomalous
32 atmospheric circulations associated with two Rossby wavetrains triggered by rising sea surface
33 temperature (SST) over the central North Pacific and the North Atlantic Oceans. On interdecadal
34 timescale, the recent increase in the occurrences of the warm Arctic-cold Eurasia pattern is a fragment
35 of the interdecadal variability of SST over the Atlantic Ocean as represented by the Atlantic
36 Multidecadal Oscillations (AMO), and over the central Pacific Ocean.

37

38 **Key words:** Warm Arctic-cold Eurasian continent, Arctic Sea ice, the Kara-Barents Sea, the
39 Self-Organizing-Map (SOM), the Pacific Decadal Oscillation (PDO), the Atlantic Multidecadal
40 Oscillation (AMO)

41

42

43

44



45 **1 Introduction**

46 In recent decades, winter season temperature in the Arctic has been rising at a rate faster than the
47 warming experienced in any other region of the world (Stroeve et al., 2007; Screen and Simmonds,
48 2010; Stroeve, 2012). In contrast, there has been an increasing trend in colder than normal winters
49 over the northern mid-latitude continents (Mori et al., 2014). This pattern of opposite winter
50 temperature trend between the Arctic and high-mid latitude continents, referred to as the warm
51 Arctic-cold continents pattern (Overland et al., 2011; Cohen et al., 2014; Walsh, 2014), has also been
52 observed on the interannual timescale (Mori et al., 2014; Kug et al., 2015). The question as to what
53 processes are responsible for the opposite change of winter air temperature between the Arctic and
54 mid-latitudes remain open (Vihma, 2014; Barnes and Screen, 2015).

55 A number of studies have attributed the recent warm Arctic-cold continents pattern to the Arctic sea
56 ice loss (Inoue et al., 2012; Tang et al., 2013; Mori et al., 2014; Kug et al., 2015; Cohen et al., 2018;
57 Mori et al., 2019). Sea ice variability in different parts of the Arctic Ocean has been linked to climate
58 variability in different parts of the world. Specifically, sea ice loss in the Barents and Kara Seas has
59 been linked to cold winters over East Asia, while a similar connection has been found between cold
60 winters in North America and sea ice retreat in the East Siberian and Chukchi Seas (Kug et al., 2015).
61 A most recent study (Matsumura and Kosaka, 2019) attributed the warm Arctic-cold continents pattern
62 to the combined effect of Arctic sea ice loss and the atmospheric teleconnection induced by tropical
63 Atlantic sea-surface temperature (SST) anomalies. Some recent studies have suggested that the
64 mid-latitude atmospheric circulation anomalies play a role in the formation of the warm Arctic-cold
65 continents pattern (Luo et al., 2016; Peings et al., 2019).

66 Other studies, however, found no cause-and-effect relationship between Arctic sea ice loss and



67 mid-latitude climate anomalies (Blackport et al., 2019; Fyfe, 2019). Numerical modeling studies using
68 coupled ocean and atmospheric models simulated no cold mid-latitude winters when the models were
69 forced with reduced Arctic sea ice cover (McCusker et al., 2016; Sun et al., 2016; Koenigk et al., 2019;
70 Blackport et al., 2019; Fyfe, 2019). The results from these studies pointed to internal atmospheric
71 variability as the likely cause for cold winters in mid-latitudes. Some studies have also suggested that
72 on the interannual timescale mid-latitude atmospheric circulation anomalies triggered by the Pacific
73 and Atlantic SST oscillations may explain both the Arctic sea ice loss and the cooling of the high-mid
74 latitudes (Lee et al., 2011; Matsumura and Kosaka, 2019; Clark and Lee, 2019). The Gulf Stream has
75 also been linked to the Barents Sea ice loss and Eurasian cooling (Sato et al., 2014).

76 Despite the recent attention given to the warm Arctic-cold continents pattern, it remains debatable as
77 to what processes may be responsible for this phenomenon. In this study, we revisit surface temperature
78 variability over the Arctic and Eurasia continent (40-90°N, 20-130°E), where the warm Arctic-cold
79 continents pattern is a prominent feature (Cohen et al., 2014; Mori et al., 2014), by applying the
80 Self-Organizing-Map (SOM) technique to daily surface temperature over the recent four decades. We
81 will show that while the warm Arctic-cold Eurasian continent pattern has dominated the recent two
82 decades, its opposite pattern, cold Arctic-warm Eurasia continent, appeared frequently in the 1980s and
83 the 90s. Using century-long data, we will further show that the warm Arctic-cold Eurasian continent
84 pattern is an intrinsic climate mode and the recent increasing trend in its occurrence is a reflection of an
85 interdecadal variability of the pattern. Using regression method, we explain the reason for the recent
86 increasing occurrences of the warm Arctic-cold continents pattern. We also assess the role of the SST
87 anomalies over the North Pacific and Atlantic Oceans in the variability of the warm Arctic-cold Eurasia
88 pattern on the interdecadal time scale.



89 2 Datasets and methods

90 From the perspective of nonlinear dynamic, a region's climate has its intrinsic modes of variability, but
91 the frequency of occurrence of these internal modes can be modulated by remote forces external to the
92 region (Palmer, 1999; Hoskins and Woollings, 2015; Shepherd, 2016). In this study we will first obtain
93 the main modes of variability of wintertime surface temperature in a region (40-90°N, 20-130°E) by
94 applying the SOM method (Kohonen, 2001) to daily surface temperature data for the 40 winters in the
95 1979-2019 period. The use of daily data over four decades allows for capturing the variability across
96 two time scales (synoptic and decadal). We will then determine, through regression and composite
97 analyses, the relationships of these modes of climate variability of surface air temperature to known
98 climate variability modes at corresponding time scales.

99 2.1 Datasets

100 Daily surface air temperature and other climate variables used in the current analyses, including 500
101 hPa geopotential height, 800-hPa wind and mean sea level pressure, all come from the European Centre
102 for Medium-Range Weather Forecasts Re-Analysis (ERA), the interim version (ERA-Interim; Dee et
103 al., 2011). Compared to the earlier versions of ERA (e.g., ERA-40, Uppala et al., 2005) and other
104 global re-analysis products (e.g. the NCEP reanalysis, Kalnay et al., 1996), ERA-Interim has been
105 found to be more accurate in portraying the Arctic warming trend (Dee et al., 2011; Screen and
106 Simmonds, 2011) despite its known warm and moist bias in the surface layer (Jakobson et al., 2012).
107 Gridded monthly SST data used in the current analysis are obtained from the US National Oceanic and
108 Atmospheric Administration (NOAA) data archives
109 (<ftp://ftp.cdc.noaa.gov/Datasets/noaa.oisst.v2.highres/>) (Reynolds et al. 2007).

110 The results obtained from the data within the recent four decades are put into the context of the



111 variability over longer time scales using data from the Twentieth Century Reanalysis project, version
112 2c (20CR) that spans more than a century from 1851 through 2015 (Compo et al., 2011). The 20CR
113 reanalysis data has a horizontal resolution of 2° latitude by 2° longitude and temporal resolution of 6
114 hours. Through the assimilation of surface observational pressure data, the 20CR reanalysis was
115 produced by the model whose lower boundary condition is derived from monthly SST and sea ice
116 conditions. Various indices used to describe known modes of climate variability are obtained from
117 NOAA's Climate prediction Center (CPC) (<https://www.esrl.noaa.gov/psd/data/climateindices/list/>),
118 which include Arctic oscillation (AO), Northern Atlantic Oscillation (NAO), Atlantic Multidecadal
119 Oscillation (AMO) (Enfield et al., 2001) and PDO (Mantua et al., 1997) indices.

120 2.2 Methods

121 The 40-year, daily surface temperature over the study region ($40\text{--}90^\circ\text{N}$, $20\text{--}130^\circ\text{E}$) is decomposed using
122 the SOM method. SOM is a clustering method based on neural network that can transform
123 multi-dimensional data into a two-dimensional array without supervised learning. The array includes a
124 series of nodes arranged by a Sammon map (Sammon, 1969). Each node in the array has a vector that
125 can represent a spatial pattern of the input data. The distance of any two nodes in the Sammon map
126 represents the level of similarity between the spatial patterns of the two nodes. Because SOM has fewer
127 limitations than most other commonly used clustering methods, (e.g., orthogonality required by the
128 empirical orthogonal function or EOF method), the SOM method can describe better the main
129 variability patterns of the input data (Reusch et al., 2005).

130 SOM method has been used in atmospheric research at mid and high latitudes of the northern
131 hemisphere (Skific et al., 2009; Johnson and Feldstein, 2010; Horton et al., 2015; Loikith and Broccoli,
132 2015; Vihma et al., 2019). For example, Johnson and Feldstein (2010) identified the spatial patterns of



133 the daily wintertime North Pacific sea level pressure and related the variability of the occurrences of
134 those patterns to some large-scale circulation indices. Loikith and Broccoli (2015) compared observed
135 and model-simulated circulation patterns across the North American domain. SOM method was used to
136 detect circulation pattern trends in a subset of North America during two periods (Horton et al., 2015).
137 In this study, the SOM method is applied to wintertime daily temperature anomalies obtained by
138 subtracting 40-year averaged daily temperature from the original daily temperature at each grid point.
139 Prior to SOM analysis, it is necessary to determine how many SOM nodes are needed to best capture
140 the variability in the data. According to previous studies (Lee and Feldstein, 2013; Gibson et al., 2017;
141 Schudeboom et al., 2018), the rule for determining the number of SOM nodes is that the number should
142 be sufficiently large to capture the variability of the data analyzed, but not too large to introduce
143 unimportant details. Table 1 shows the averaged spatial correlation between all daily surface air
144 temperature and their matching nodes. There is an increase in correlation coefficients from 0.26 for a
145 3×1 grid to 0.51 for a 4×4 grid, but the gain from a 3×3 grid to a 4×4 grid is relatively small. Hence, a
146 3×3 grid seems to meet the above-mentioned rule and will be utilized in this study.

147 The contribution of each SOM node to the trend in wintertime surface temperature is calculated by
148 the product of each node pattern and its frequency trend normalized by the total number of wintertime
149 days (90, Lee and Feldstein, 2013). The sum of the contributions from all nodes denotes the
150 SOM-explained trends. Residual trends are equal to the subtraction of SOM-explained trends from the
151 total trends. The statistical significance in this study is tested by using the Student's t test.

152 **3 Results**

153 3.1 Surface temperature variability

154 The majority of the 9 SOM nodes depict a dipole pattern characterized by opposite changes in surface



155 temperature between the Arctic Ocean and the Eurasian continent, although the sign switch does not
156 always occur at the continent-ocean boundary (Figure 1). The position of the boundary between the
157 warm and cold anomalies reflect the transition between the cold Arctic-warm Eurasia pattern (denoted,
158 in descent order of the occurrence frequency, by nodes 3, 9, 6), to the warm Arctic-cold Eurasia pattern
159 (depicted, in descent order of the occurrence frequency, by nodes 1, 7, 4). The spatial patterns
160 represented by the first group of nodes (3, 9, 6) are almost mirror images of the patterns denoted by the
161 corresponding nodes in the second group (1, 7, 4). For example, the first node in group 1 (node 9,
162 15.4%) and in group 2 (node 1, 17.1%) show a mirror image pattern with cold (warm) anomalies in the
163 Arctic Ocean extending into northern Eurasia and warm (cold) anomalies in the rest of the Eurasia
164 continent in the study domain. In both cases, the region of maximum anomalies is centered near
165 Svalbard, Norway. The second most frequent pattern, denoted by node 3 (17.2%) and 7 (13.7%) in the
166 two groups, respectively, has the boundary of separation moved northward from northern Eurasia
167 continent toward the shore of the Arctic Ocean. While the maximum anomaly in the Arctic Ocean
168 remains close to Svalbard, maximum values over the continent are found in central Russia. Nodes 4-6
169 display a noticeable transition from node 1 to node 7 and from node 3 to node 9, respectively. Although
170 nodes 2 and 8 show an approximate monopole spatial pattern, they also represent a transition between
171 nodes 1 and 3, and between nodes 7 and 9, respectively. Above SOM analysis cannot consider the trend
172 in surface air temperature. The result is similar while removing the trend (Not shown).

173 The temporal variability on this time scale is typically related to synoptic processes and hence the
174 questions are what synoptic patterns are responsible for the occurrence of the spatial patterns depicted
175 by each of the 9 SOM nodes and how these patterns are related to those of the Arctic sea ice anomalies?
176 These questions can be answered by using the composite method. Specifically, for each node,



177 composite maps are made respectively for the anomalous 500-hPa geopotential height, mean sea level
178 pressure, 850-hPa wind, downward longwave radiation, surface turbulent heat flux, and sea ice
179 concentration over all the days when the spatial variability of the surface temperature anomalies is best
180 matched by the spatial pattern of that node.

181 3.2 Large-scale circulation patterns

182 For all nodes, the spatial pattern of the composited 500 hPa-geopotential height anomalies (Figure 2) is
183 similar to that of mean sea level pressure anomalies (Not shown), indicating an approximately
184 barotropic structure. For nodes 1, 4 and 7, 500-hPa height anomalies show a dipole structure of positive
185 values over Siberia and negative values to its south. Anomalous southwesterly winds on the western
186 side of the anticyclone over Siberia transport warm and moist air from northern Europe and the North
187 Atlantic Ocean into the Atlantic sector of the Arctic Ocean (Figure 3), providing a plausible
188 explanation of the warm surface temperature anomalies in the region (Figure 1). On the eastern side of
189 the anticyclone, anomalous northwesterly winds bring cold and dry air from the Arctic Ocean into
190 Eurasia continent, which is consistent with the negative surface temperature anomalies there. The
191 opposite occurs for nodes 3, 6 and 9. A similar explanation involving anomalous pressure and wind
192 fields can be applied to other nodes. The dipole structure that dominates the anomalous 500-hPa height
193 fields over the North Atlantic Ocean for most nodes resembles the spatial pattern of the NAO. In
194 addition, the patterns for a few nodes, such as nodes 4 and 7, have some resemblance to the spatial
195 pattern of the AO over larger geographical region. The possible connection to NAO and AO is further
196 investigated by averaging the daily index values of NAO or AO over all occurrence days for each node.
197 The results (Table 2) show that nodes 1, 2, 3 (5, 8, 9) correspond to a significant positive (negative)
198 phase of the NAO index characterized by negative (positive) height anomalies over Iceland and



199 positive (negative) values over the central North Atlantic Ocean. Association is also found between
200 nodes 1, 2, 3, and 6 (5, 7, 8, and 9) and the positive (negative) phases of the AO index.

201 3.3 Downward radiative fluxes

202 Besides the anomalous circulation patterns, anomalous surface radiative fluxes may also play a role in
203 shaping the spatial pattern of surface temperature variability. In fact, the spatial pattern of the mean
204 anomalous daily downward longwave radiation for an individual node (Figure 4) is in good agreement
205 with the spatial pattern of the surface temperature anomalies of that node. In other words, increased
206 downward longwave radiation is associated with positive surface temperature anomalies, and vice
207 versa. As expected from previous studies (e.g., Sedlar et al. 2011), there is a significant positive
208 correlation between downward longwave radiative fluxes and the anomalous total column water vapor
209 and mid-level cloud cover (not shown). The correlation to low- and high-level cloud cover is, however,
210 not significant (Not shown). Most of the water vapor in both the Arctic and Eurasia is derived from the
211 North Atlantic Ocean, but the water vapor is transported into the Arctic by southwesterly flows and into
212 Eurasia by northwesterly winds. The anomalous shortwave radiation corresponding to each node (not
213 shown) is an order of magnitude smaller than that of the longwave radiation anomalies and has a spatial
214 pattern opposite to that of the mid-level cloud cover and the longwave radiation anomalies.

215 3.4 Sea ice

216 The analyses presented above attempt to explain the spatial pattern of surface temperature variability
217 for each node from the perspective of anomalous heat advection and surface radiative fluxes. As
218 mentioned earlier, there has been a debate in the literature about the role played by the sea ice
219 anomalies in the Barents and Kara Seas in the development of the warm Arctic-cold Eurasia pattern.
220 Here, we examine the anomalous turbulent heat flux (Figure 5) and sea ice concentration (Figure 6) for



221 each node. Turbulent heat flux is considered positive when it is directed from the atmosphere
222 downward to the ocean or land surfaces. Thus, a positive anomaly indicates either an increase in the
223 atmosphere-to-surface heat transfer or a decrease in the heat transfer from the surface to the atmosphere.
224 The magnitude of anomalous turbulent heat flux is found to be comparable to that of anomalous
225 downward longwave radiation (Figure 4). For all nodes, the heat flux anomalies are larger over ocean
226 than over land. For node 1, positive turbulent heat flux anomalies occur mainly over the Barents Sea,
227 the western and central North Atlantic Ocean and the eastern North Pacific Ocean, indicating an
228 increase in heat transport from the air to the ocean due possibly to an increase in vertical temperature
229 gradient caused by warm air advection associated with anomalous circulation. The downward heat
230 transfer results in sea ice melt in the Greenland Sea and the Barents Sea (Figure 6). For node 4, the
231 anomalous southerly winds over the Nordic Sea produce larger positive turbulent heat flux anomalies.
232 For node 7, the anticyclone is located more northwards, which generates opposite anomalous winds
233 between the Nordic and northern Barents Seas and the southern Barents Sea and thus opposite turbulent
234 heat flux anomalies that are consistent with the opposite sea ice concentration anomalies in the two
235 regions. For nodes 3, 6, and 9, the anomalous cold air from the central Arctic Ocean flows into warm
236 water in the Nordic and Barents Seas, producing negative turbulent heat flux anomalies and positive
237 sea ice concentration anomalies. Sorokina et al. (2016) noted that turbulent heat flux usually peaks 2
238 days before changes in surface temperature pattern occur. The pattern of the composted anomalous
239 turbulent heat flux 2 days prior to the day when the nodes occur (not shown) is similar to the
240 current-day pattern in Figure 6. Our results support the conclusion of Sorokina et al. (2016) and
241 Blackport et al. (2019) that the anomalous atmospheric circulations lead to the anomalous sea ice
242 concentration in the Barents Sea.



243 3.5 Contributions of SOM nodes to the trends in wintertime surface temperature

244 The results above suggest that both the surface temperature anomaly patterns over the Arctic Ocean and
245 Eurasian continent and the sea ice concentration anomalies in the Nordic and Barents Seas can be
246 explained largely by changes in atmospheric circulations and the associated vertical and horizontal heat
247 and moisture transfer by mean and turbulent flows. Next, we assess the contributions of these nodes to
248 the trend in wintertime surface temperature.

249 We first examine the time series of the accumulated number of days for each node in each winter for
250 the 1979-2019 period (Figure 7). The time series for nodes 1, 4, 6, and 9 exhibit variability on
251 interannual as well as decadal time scales. The occurrence frequency is noticeably larger after 2003
252 than prior to 2003 for nodes 1 and 4, and vice versa for nodes 6 and 9, and the difference between the
253 two periods is significant at 95% confidence level. Given the spatial patterns of these four nodes
254 (Figure 1), this indicates that the warm Arctic-cold Eurasia pattern occurred more frequently after 2003.
255 A linear trend analysis of the time series for each node (Table 2) reveals significant positive trends in
256 occurrence frequency for nodes 1 and 4 and significant negative trends for nodes 6 and 9, which agree
257 with the result from a previous study (Clark and Lee, 2019) that suggested an increasing trend of the
258 warm Arctic and cold Eurasia pattern.

259 These trends in the occurrence frequency of the SOM nodes contribute to the trends in the total
260 wintertime (DJF) surface temperature anomalies (Figure 8, top panel) that have significant positive
261 trends over the Arctic Ocean and in regions of Northern and Southern Europe and negative trends in
262 Central Siberia. The contribution, however, varies from node to node (Figure 9). Node 1 has the largest
263 domain-averaged contribution of 18.7%, followed by its mirror node (node 9) at 10.1%. Nodes 4 and 6
264 account for 2.8% and 4.3% of the total trend, respectively. None of the remaining nodes explain more



265 than 2%. All nodes together explain 39.5% of the total trend in wintertime surface air temperature. The
266 spatial pattern of the SOM-explained trends (Figure 8, middle panel) is similar to the warm
267 Arctic--cold continent pattern, whereas the residual trend resembles more the total trend (Figure 8
268 bottom panel).

269 3.6 Mechanisms

270 The results presented above indicate that the SOM patterns explain nearly 40% of the trend in
271 wintertime surface air temperature anomalies and majority of the contributions (35 out of 40%) come
272 from the two pairs of the nodes (nodes 1, 9, and 4, 6). The analyses hereafter will focus on these four
273 nodes. Below we assess the atmospheric and oceanic conditions associated with the occurrences of the
274 four nodes via regression analysis. Specifically, the anomalous seasonal SST and atmospheric
275 circulation variables are regressed onto the normalized time series of the number of days when each of
276 the four nodes occurs (Figures 10, 11, and 12).

277 For node 1, the SST regression pattern in the Pacific Ocean shows significant positive anomalies
278 over the tropical western Pacific Ocean and central North Pacific Ocean. The positive SST anomalies
279 also occur over most of the North Atlantic. Negative SST anomalies occur over the central tropical
280 Pacific Ocean, though they are not significant at 95% confidence level. The SST regression pattern is
281 reversed for node 9. The corresponding anomalous 500-hPa height regression shows two Rossby
282 wavetrains: one is excited over the central Pacific Ocean and propagates northeastwards into North
283 America and North Atlantic Ocean, and the other, which displays the stronger signal, originates from
284 central North Atlantic and propagates northeastwards to the Arctic Ocean and southeastwards to the
285 Eurasian continent and the western Pacific Ocean. The large SST anomalies over the Nordic Ocean
286 augment the wave signal through local air-sea interaction. The wave activity flux and streamfunction



287 exhibit well the horizontal propagating direction of the planetary wave. For node 9, the corresponding
288 anomalous 500-hPa height and streamfunction show an opposite pattern, but the wave activity flux is
289 similar to that of node 1.

290 For node 4, the SST anomalies over the tropical Pacific Ocean appear to be in a La Niña state, which
291 shows stronger negative SST anomalies over the eastern tropical Pacific Ocean than those for node 1.
292 The positive SST anomalies over the North Pacific shift more northwards relative to that of node 1. The
293 positive SST anomalies over the North Atlantic are weaker than those for node 1. The corresponding
294 wavetrain over the Pacific Ocean is stronger than that over the Atlantic Ocean, which can also be
295 observed in the pattern of wave activity and streamfunction. The corresponding pattern for node 6 is
296 nearly reversed, but there are some noticeable differences in the amplitude of the wavetrain and SST
297 anomalies. For example, the magnitude of the anomalous SST and the 500-hPa height over the central
298 North Pacific is larger for node 6 than that for node 4.

299 Besides the above-mentioned variables, similar regression analysis is also performed for the
300 anomalous 850-hPa wind field and anomalous downward longwave radiation (Not shown). Their
301 regression patterns, which are similar to those in Figures 3 and 4, explain well the decadal variability of
302 the number of days for nodes 1, 4, 6, and 9. Together, these results indicate that the decadal variability
303 of the occurrence frequency of the four nodes in recent decades is related to two wavetrains induced by
304 SST anomalies over the central North Pacific Ocean and the North Atlantic Ocean. The aforementioned
305 SST regression patterns over the Atlantic and Pacific Oceans also show features of the AMO and PDO
306 (Figure 10). Since both the AMO and PDO exhibited a phase change in the late 1990s (Yu et al., 2017),
307 the question is whether a similar change in the SOM frequency also appear in the late 1990s. A
308 comparison of the averaged frequency before and after 1998 shows a significant drop in frequency for



309 nodes 6 and 9 and an increase in frequency for node 1. This result suggests that the change in the AMO
310 and PDO indices may contribute to the change in the frequencies of the warm Arctic-cold Eurasia
311 continent pattern.

312 3.7 Interdecadal variability

313 The four-decade-long ERA-Interim reanalysis is not adequate for examining interdecadal to
314 multi-decadal variations represented by the PDO and AMO indices. Further analysis is performed using
315 the 20CR daily reanalysis data for the 1854-2014 period. Before applying the SOM technique to the
316 20CR data, we first remove the trend to eliminate the influence from the global warming. No low-pass
317 filter is applied before SOM analysis in order to test the stability of the SOM results for the different
318 periods. The spatial SOM patterns from the de-trended century-long 20CR data (Figure 13) are similar
319 to those for the 1979-2019 period (Figure 1). Nodes 1, 4, and 7 correspond to the positive phase of the
320 warm Arctic-cold Eurasia pattern and the negative phase can be observed in nodes 3, 6, and 9. The
321 magnitude is smaller compared to the recent four decades. The occurrence frequencies of all the nodes
322 (Figure 14) are close to those for the recent four decades. It indicates that the SOM method can obtain
323 stably the main modes of wintertime surface air temperature variability. For the recent four decades, the
324 time series of the number of days also displays a noticeable increasing (decreasing) trend for nodes 1
325 and 4 (6 and 9), suggesting that the trend in the recent four decades is a reflection of an interdecadal
326 variability of wintertime surface air temperature.

327 Next, we apply a 40-year low-pass filter to the time series of the occurrence frequencies for nodes 1,
328 4, 6 and 9 and the AMO and PDO indices and calculate correlations. There is a significant correlation
329 between the time series and the AMO index, with correlation coefficients of 0.36 for node 1, 0.27 for
330 node 4, -0.37 for node 6, and -0.20 for node 9, all of which are at the 95% confidence level. No



331 significant correlations, however, are found between the filtered time series and the PDO index. If we
332 define an SST index to represent the variability of SST anomalies over the central North Pacific Ocean
333 (20°N–40°N, 150°E–150°W), the 40-year low-pass filtered central North Pacific Ocean SST index is
334 now significantly correlated with the filtered time series of occurrence frequencies for nodes 1 and 9
335 (0.55 for node 1 and -0.46 for node 9). The results are consistent with the SST regression map for the
336 recent decades (Figure 10).

337 To confirm the effect of SST anomalies on the warm Arctic -cold Eurasia pattern, we also perform
338 EOF analysis of wintertime detrended seasonal surface air temperature anomalies for the 1854–2014
339 period (Figure 15). The spatial patterns of the first and second EOF modes show the negative phase of
340 the warm Arctic-cold Eurasia pattern and the 40-year low-pass filtered time series is inversely
341 correlated with the 40-year low-pass filtered wintertime AMO index (-0.46 $p < 0.05$ for mode 1 and
342 -0.44 $p < 0.05$ for mode 2). The 40-year low-pass filtered time series of the two EOF modes has a
343 significant negative correlation with the 40-year low-pass filtered central North Pacific Ocean SST
344 index, with correlation coefficients of -0.19 and -0.26 ($p < 0.05$). Only PC1 has a significant correlation
345 with the PDO index (0.38 $p < 0.05$). Thus, the increase in the occurrence of the warm Arctic-cold
346 Eurasia pattern in the recent decades is a part of the interdecadal variability of the pattern, which is
347 influenced by the AMO index and the central North Pacific SST.

348 **4 Conclusions and Discussions**

349 In this study, we examine the variability of wintertime surface air temperature in the Arctic and the
350 Eurasian continent (20°E–130°E) by applying the SOM method to daily temperature from the gridded
351 ERA-Interim dataset for the period 1979–2019 and from the 20CR reanalysis for the period 1854–2014
352 and the EOF method to seasonal temperature from the 20CR reanalysis for the period 1854–2014.



353 The spatial pattern in the surface temperature variations in the study region, as revealed by the nine
354 SOM nodes, is dominated by concurrent warming in the Arctic and cooling in Eurasia, and vice versa.
355 The nine SOM patterns explain nearly 40% of the trends in wintertime surface temperature and 88% of
356 that are accounted for by only four nodes. Two of the four nodes (nodes 1 and 4) represent the warm
357 Arctic-cold Eurasian pattern and the other two (nodes 6 and 9) depict the opposite cold Arctic-warm
358 Eurasia pattern. There is a clear shift in the frequency of the occurrence of these patterns near the
359 beginning of this century, with the warm Arctic – cold Eurasia pattern dominating since 2003, while the
360 opposite pattern prevailing from the 1980s through the 1990s. The warm Arctic-cold Eurasia pattern is
361 accompanied by an anomalous high pressure and anticyclonic circulation over the Eurasian continent.
362 The anomalous winds and the associated temperature and moisture advection interact with local
363 longwave radiative forcing and turbulence to produce positive (negative) temperature anomalies in the
364 Arctic (Eurasian continent). The circulation is reversed for the cold Arctic-warm Eurasia pattern. The
365 warm, moist air mass advected to the Arctic by the anomalous atmospheric circulations and the
366 increased downward turbulent heat flux also explain sea ice melt in the Barents and Kara Seas. In other
367 words, the sea ice loss in the Barents and Kara Seas and the cooling of the Eurasian continent can both
368 be traced to anomalous atmospheric circulations.

369 Increasing occurrences of the warm Arctic-cold Eurasian continent pattern appear to relate to rising
370 SST over the central North Pacific and North Atlantic Oceans (positive AMO phase). The SST
371 anomalies trigger two Rossby wavetrains spanning from the North Pacific Ocean, North America, and
372 the North Atlantic Ocean to the Eurasian continent. The two wavetrains are strengthened through local
373 sea-atmosphere-ice interactions in mid-high latitudes, which influence the change in the occurrence
374 frequency of the warm Arctic-cold Eurasian continent pattern. Our results agree with those of previous



375 studies (Lee et al., 2011; Sato et al., 2014; Clark and Lee, 2019). But previous studies only focus on the
376 effect of SST anomalies over either North Pacific or North Atlantic Oceans. We also note that the two
377 wavetrains excited by SST anomalies over different oceans differ in amplitudes, leading to somewhat
378 different warm Arctic-cold Eurasia patterns.

379 Using century-long data, we show that the warm Arctic-cold Eurasia pattern is an intrinsic climate
380 mode, which has been stable since 1854. The recent increasing trend in its occurrence is a reflection of
381 an interdecadal variability of the pattern resulting from the interdecadal variability of SST anomalies
382 over the central Pacific Ocean and over the Atlantic Ocean represented by the AMO index. Sung et al.
383 (2018) investigated interdecadal variability of the warm Arctic and cold Eurasia pattern and considered
384 the variability of the SST over the North Atlantic as its origin. Our results suggest that the variability of
385 the SST over the North Pacific also plays an important role. However, internal atmospheric variability
386 remains another potential source. The Rossby wavetrains also lead to deepening of a trough in East
387 Asia and generate an anomalous low and cold temperature in northern China, which further suggests
388 that the relationship between a warmer Arctic, especially warmer Barents and Kara Seas, and the
389 occurrence of cold spells in East Asia may not be as strong as previously thought (Kim et al., 2014;
390 Mori et al., 2014; Kug et al., 2015; Overland et al., 2015).

391 Our results help broaden the current understanding of the formation mechanisms for the warm
392 Arctic-cold Eurasia pattern. The SST anomalies over Northern Hemisphere oceans may offer a
393 potential for predicting its occurrence.

394 **Data Availability**

395 All data used in the current analyses are publicly available. The monthly sea ice concentration data are
396 available from the National Snow and Ice Data Center (NSIDC) (<http://nsidc.org/data/NSIDC-0051>), the
397 ERA-Interim reanalysis data are available from the European Center for Mid-Range Weather



398 Forecasting (<https://www.ecmwf.int/en/forecasts/datasets/reanalysis-datasets/era-interim>) and the sea
399 surface temperature data are available from the Hadley Centre for Climate Prediction and Research
400 (<ftp://ftp.cdc.noaa.gov/Datasets/noaa.oisst.v2.highres/>). The long-term SST data are derived from
401 from the Twentieth Century Reanalysis project, version 2c (20CR)
402 (<https://climatedataguide.ucar.edu/climate-data/noaa-20th-century-reanalysis-version-2-and-2c>).

403 **Competing interests**

404 The authors declare that they have no conflict of interest.

405 **Author Contributions**

406 L. Yu designed the study, with input from S. Zhong, and carried out the analyses. L. Yu and S. Zhong
407 prepared the manuscript. C. Sui plotted a part of Figures.

408 **Acknowledgements** We thank the European Centre for Medium-Range Weather Forecasts (ECMWF)
409 for the ERA-Interim data. This study is financially supported by the National Key R&D Program of
410 China (2019YFC1509102; 2017YFE0111700) and the National Natural Science Foundation of China
411 (41922044).

412

413

414

415

416

417

418

419

420

421

422



423

424 **References**

425 Barnes, E. A. and Screen, J. A.: The impact of Arctic warming on the midlatitude jet-stream: Can it?

426 Has it? Will it?, *WIREs Clim. Change*, 6, 277-286, doi:10.1002/wcc.337, 2015.

427 Blackport, R., Screen J. A., Wiel K. van der, and Bintanja, R.: Minimal influence of reduced Arctic sea

428 ice on coincident cold winters in mid-latitudes, *Nature Climate Change*, 9,

429 doi:10.1038/s41558-019-0551-4, 2019, 2019.

430 Clark, J. P. and Lee, S.: The role of the tropically excited Arctic Warming Mechanism on the warm

431 Arctic cold continent surface air temperature trend pattern, *Geophys. Res. Lett.*, 46, 8490-8499,

432 doi:10.1029/2019GL082714, 2019

433 Cohen, J., Screen, J. A., Furtado, J. C., Barlow, M., Whittleston, D., Coumou, D., Francis, J., Dethloff,

434 K., Entekhabi, D., Overland, J., and Jones, J.: Recent Arctic amplification and extreme

435 mid-latitude weather, *Nat. Geosci.*, 7, 627-637, doi:10.1038/ngeo2234, 2014.

436 Cohen, J., Pfeiffer, K., and Francis, J. A.: Warm Arctic episodes linked with increased frequency of

437 extreme winter weather in the United States, *Nat. Commun.*, 9, 869,

438 doi:10.1038/s41467-018-02992-9, 2018.

439 Compo, G. P., Whitaker, J. S., Sardeshmukh, P. D., Matsui, N., Allan, R., Yin, X., Jr, G. B. E., Vose, R.

440 S., Rutledge, G. K., Bessemoulin, P., Brönnimann, S., Brunet, M., Crouthamel, R. I., Grant, A.

441 N., Groisman, P. Y., Jones, P. D., Kruk, M. C., Kruger, A. C., Marshall, G. J., Maugeri, M., Mok,

442 H. Y., Nordli, Ø., Ross, T. F., Trigo, R. M., Wang, X., Woodruff, S. D., and Worley S. J.: The

443 Twentieth Century Reanalysis Project, *Quart. J. Roy. Meteor. Soc.*, 137, 1-28,

444 doi:10.1002/qj.776, 2011.



- 445 Dee, D. P., Uppala, S. M., Simmons, A. J., Berrisford, P., Poli, P., Kobayashi, S., Andrac, U.,
446 Balmaseda, M. A., Balsamo, G., Bauer, P., Bechtold, P., Beljaars, A. C. M., van de Berg, L.,
447 Bidlot, J., Bormann, N., Delsol, C., Dragani, R., Fuentes, M., Geer, A. J., Haimberger, L., Healy,
448 S. B., Hersbach, H., Hólm, E. V., Isaksen, I., Kållberg, P., Köhler, M., Matricardi, M., McNally, A.
449 P., Monge-Sanz, B. M., Morcrette, J.-J., Park, B.-K., Peubey, C., de Rosnay, P., Tavolato, C.,
450 Thépaut, J.-N., and Vitart, F.: The ERA-Interim reanalysis: configuration and performance of the
451 data assimilation system. *Q. J. R. Meteorol. Soc.*, 137, 553-597, doi:10.1002/qj.828, 2011.
- 452 Enfield, D. B., Mestas-Nunez, A. M., and Trimble, P. J.: The Atlantic multidecadal oscillation and its
453 relation to rainfall and river flows in the continental U.S., *Geophys. Res. Lett.*, 28, 2077-2080,
454 2001.
- 455 Fyfe, J. C.: Midlatitudes unaffected by sea ice loss. *Nature Climate Change*, 9,
456 doi:10.1038/s41558-019-0560-3, 2019 .
- 457 Gibson, P. B., Perkins-Kirkpatrick, S. E., Uotila, P., Pepler, A. S., and Alexander, L. V.: On the use of
458 self-organizing maps for studying climate extremes, *J. Geophys. Res. Atmos.*, 122, 3891–3903,
459 [doi:10.1002/2016JD026256](https://doi.org/10.1002/2016JD026256), 2017.
- 460 Hoskins, B. and Woollings, T.: Persistent extratropical regimes and climate extremes. *Curr. Clim. Change*
461 *Rep.*, 1, 115-124, doi:10.1007/s40641-015-0020-8, 2015
- 462 Horton, D. E., Johnson, N. C., Singh, D., Swain, D. L., Rajaratnam, B., and Diffenbaugh, N. S.:
463 Contribution of changes in atmospheric circulation patterns to extreme trends, *Nature*,
464 522,465-469, doi:10.1038/nature14550, 2015.
- 465 Inoue, J., Hori, M. E., and Takaya, K.: The role of Barents Sea ice in the wintertime cyclone track and
466 emergence of a warm-Arctic-Siberian anomaly, *J. Clim.*, 25, 2561-2568,



- 467 doi:10.1175/JCLI-D-11-00449.1, 2012.
- 468 Jakobson, E., Vihma, T., Palo, T., Jakobson, L., Keernik, H., and Jaagus, J.: Validation of atmospheric
469 reanalyses over the central Arctic Ocean, *Geophys. Res. Lett.*, 39, L10802,
470 doi:10.1029/2012GL051591, 2012.
- 471 Johnson, N. C. and Feldstein, S. B.: The continuum of North Pacific sea level pressure patterns:
472 Intraseasonal, interannual, and interdecadal variability, *J. Clim.*, 23,
473 851-867, doi:10.1175/2009JCLI3099.1, 2010.
- 474 Kalnay, E., Kanamitsu, M., Kistler, R., Collins, W. G., Deaven, D., Gandin, L., Iredell, M., Saha, S.,
475 White, G., Woollen J.: The NCEP/NCAR 40-year reanalysis project, *Bull. Amer. Meteor. Soc.*,
476 77, 437-471, doi:10.1175/1520-0477(1996)077<0437:TNYRP>2.0.CO;2, 1996.
- 477 Kim, B.-M., Son, S.-W., Min, S.-K., Jeong, J.-H., Kim, S.-J., Zhang, X., Shim, T., and Yoon, J.-H.:
478 Weakening of the stratospheric polar vortex by Arctic sea-ice loss, *Nature Commun.*, 5, 4646,
479 doi:10.1038/ncomms5646, 2014.
- 480 Kohonen, T.: *Self-Organizing Maps*. 3rd ed. Springer, 501 pp, 2001.
- 481 Kug, J.-S., Jeong, J.-H., Jang, Y.-S., Kim, B.-M., Folland, C. K., Min, S.-K., and Son, S.-W.: Two
482 distinct influences of Arctic warming on cold winters over North America and East Asia, *Nat.*
483 *Geosci.*, 8, 759-762, doi:10.1038/ngeo2517, 2015.
- 484 Lee, S., Gong, T., Johnson, N., Feldstein, S. B., and Pollard, D.: On the possible link between tropical
485 convection and the Northern Hemisphere Arctic surface air temperature change between 1958
486 and 2001, *J. Clim.*, 24, 4350-4367, doi:10.1175/2011JCLI4003.1, 2011.
- 487 Lee, S. and Feldstein, S. B.: Detecting ozone- and greenhouse gas-driven wind trends with
488 observational data, *Science*, 339, 563-567, doi:10.1126/science.1225154, 2013.



- 489 Loikith, P. C. and Broccoli, A. J.: Comparison between observed and model-simulated atmospheric
490 circulation patterns associated with extreme temperature days over North America using CMIP5
491 historical simulations, *J. Clim.*, 28, 2063-2079, doi:10.1175/JCLI-D-13-00544.1, 2015.
- 492 Luo, D., Xiao, Y., Yao, Y., Dai, A., Simmonds, I., and Franzke, C. L. E.: Impact of Ural blocking on
493 winter warm Arctic-cold Eurasian anomalies. Part I: Blocking-induced amplification, *J. Clim.*,
494 29, 3925-3947, doi:10.1175/JCLI-D-15-0611.1, 2016.
- 495 Mantua, N. J., Hare, S. R., Zhang, Y., Wallace, J. M., and Francis, R. C.: A Pacific interdecadal climate
496 oscillation with impacts on salmon production, *Bull. Amer. Meteor. Soc.*, 78, 1069–1079, 1997.
- 497 Matsumura, S. and Kosaka, Y.: Arctic-Eurasian climate linkage induced by tropical ocean variability,
498 *Nature Communications*, 10, 3441, doi:10.1038/s41467-019-11359-7, 2019.
- 499 Mori, M., Watanabe, M., Shiogama, H., Inoue, J., and Kimoto, M.: Robust Arctic sea-ice influence on
500 the frequent Eurasian cold winters in past decades, *Nat. Geosci.*, 7, 869-873,
501 doi:10.1038/ngeo2277, 2014.
- 502 Mori, M., Kosaka, Y., Watanabe, M., Nakamura, H., and Kimoto, M.: A reconciled estimate of the
503 influence of Arctic sea-ice loss on recent Eurasian cooling, *Nat. Clim. Change*, 9, 123-129,
504 doi:10.1038/s41558-018-0379-3, 2019.
- 505 McCusker, K. E., Fyfe, J. C., and Sigmond, M.: Twenty-five winters of unexcepted Eurasian cooling
506 unlikely due to Arctic sea-ice loss, *Nat. Geosci.*, 9, 838-842, doi:10.1038/ngeo2820, 2016.
- 507 Overland, J. E., Wood, K. R., and Wang, M.: Warm Arctic-cold continents: climate impacts of the
508 newly open Arctic sea, *Polar Res.*, 30, 15787, doi:10.3402/polar.v30i0.15787, 2011.
- 509 Overland, J. E., Francis, J., Hall, R., Hanna, E., Kim, S.-J., and Vihma, T.: The melting Arctic and
510 Midlatitude weather patterns: Are they connected?, *J. Clim.*, 28, 7917-7932,



- 511 doi:10.1175/JCLI-D-14-00822.1, 2015.
- 512 Palmer, T. N.: A nonlinear dynamical perspective on climate prediction, *J. Clim.*, 12, 575-591, 1999.
- 513 doi:10.1175/1520-0442(1999)012<0575:ANDPOC>2.0.CO;2
- 514 Peings, Y.: Ural blocking as a driver of early-winter stratospheric warmings, *Geophys. Res. Lett.*, 46,
- 515 5460-5468, doi:10.1029/2019GL082097, 2019.
- 516 Reusch, D. B., Alley, R. B., and Hewitson, B. C.: Relative performance of self-organizing maps and
- 517 principal component analysis in pattern extraction from synthetic climatological data, *Polar*
- 518 *Geogr.*, 29, 188–212, doi:10.1080/789610199, 2005.
- 519 Reynolds, R. W., Smith, T. M., Liu, C., Chelton, D. B., Casey, K. S., Schlax, M. G.: Daily
- 520 High-Resolution-Blended Analyses for Sea Surface Temperature, *J. Climate*, 20, 5473-5496,
- 521 doi:10.1175/2007JCLI1824.1, 2007.
- 522 Sammon, J. W.: A non-linear mapping for data structure analysis. *IEEE Trans. Computers*, C-18,
- 523 401–409 , 1969.
- 524 Sato, K., Inoue, J., and Watanabe, M.: Influence of the Gulf Stream on the Barents Sea ice retreat and
- 525 Eurasian coldness during early winter, *Environ. Res. Lett.*, 9, 084009,
- 526 doi:10.1088/1748-9326/9/8/084009, 2014.
- 527 Schudeboom, A., McDonald, A. J., Morgenstern, O., Harvey, M., and Parsons, S.: Regional
- 528 regime-based evaluation of present-day GCM cloud simulations using self-organizing maps, *J.*
- 529 *Geophys. Res. Atmos.*, 123, 4259–4272, doi:10.1002/2017JD028196, 2018.
- 530 Screen, J. A. and Simmonds, I.: The central role of diminishing sea ice in recent Arctic temperature
- 531 amplification, *Nature*, 464, 1334-1337, doi:10.1038/nature09051, 2010.
- 532 Screen, J. S. and Simmonds, I.: Erroneous Arctic temperature trends in the ERA-40 reanalysis: A closer



- 533 look, *J. Clim.*, 24, 2620–2627, doi:10.1175/2010JCLI4054.1, 2011.
- 534 Sedlar, J., Tjernström, M., Mauritsen, T., Shupe, M. D., Brooks, I. M., PPerson, O., Birch, C. E., Leck,
535 C., Sirevaag, A., and Nicolaus, M. : A transitioning Arctic surface energy budget: The impacts of
536 solar zenith angle, surface albedo and cloud radiative forcing, *Clim. Dyn.*, 37, 1643–1660,
537 [doi:10.1007/s00382-010-0937-5](https://doi.org/10.1007/s00382-010-0937-5), 2011.
- 538 Shepherd, T. G.: Effects of a warming Arctic, *Science*, 353, 989-990, doi:10.1126/science.aag2349,
539 2016.
- 540 Skific, N., Francis, J. A., and Cassano, J. J.: Attribution of projected changes in atmospheric moisture
541 transport in the Arctic: A self-organizing map perspective, *J. Clim.*, 22, 4135-4153,
542 doi:10.1175/2009JCLI2645.1, 2009.
- 543 Sorokina, S. A., Li, C., Wettstein, J. J., and Kvamstø N. G.: Observed atmospheric coupling between
544 Barents sea ice and the warm-Arctic cold-Siberian anomaly pattern, *J. Clim.*, 29, 495-511,
545 doi:10.1175/JCLI-D-15-0046.1, 2016.
- 546 Stroeve, J. C., , Holland, M. M., Meier, W., Scambos, T., and Serreze, M.: Arctic sea ice decline: faster
547 than forecast, *Geophys. Res. Lett.*, 34, L09051, doi:10.1029/2007gl029703, 2007.
- 548 Stroeve, J. C.: Trends in Arctic sea ice extent from CMIP5, CMIP3 and observations, *Geophys. Res.*
549 *lett.*, 39, L16502, doi:10.1029/2012GL052676 , 2012.
- 550 Sun, L., Perlwitz, J., and Hoerling, M.: What caused the recent “warm Arctic-Cold Continents” trend
551 pattern in winter temperature?, *Geophys. Res. Lett.*, 43, 5345-5352,
552 doi:10.1002/2016GL069024, 2016.
- 553 Sung, M.-K., Kim, S.-H., Kim, B.-M., and Choi, Y.-S.: Interdecadal variability of the warm Arctic and
554 cold Eurasia pattern and its North Atlantic origin, *Journal of Climate*, 31, 5793-5810,



- 555 doi:10.1175/JCLI-D-17-0562.1, 2018.
- 556 Tang, Q., Zhang, X., Yang, X., and Francis J. A.: Cold winter extremes in northern conditions linked to
557 Arctic sea ice loss, *Environ. Res. Lett.*, 8, 014036, doi:1088/1748-9326/8/1/014036 ,2013.
- 558 Uppala, S., KÅllberg, P. W., Simmons, A. J., Andrae, U., Da Costa Bechtold, V., Florino, M., Gibson, J.
559 K., Haseler, J., Hernandez, A., Kelly, G. A., Li, X., Onogi, K., Saarinen, S., Sokka, N., Allan, R.
560 P., Andersson, E., Arpe, K., Balmaseda, M. A., Beljaars, A. C. M., Van De Berg, L., Bidlot, J.,
561 Bormann, N., Caires, S., Chevallier, F., Dethof, A., Dragosavac, M., Fisher, M., Fuentes, M.,
562 Hagemann, S., Hølm, E., Hoskins, B. J., Isaksen, L., Janssen, P. A. E. M., Jenne, R., McNally, A.
563 P., Mahfouf, J.-F., Morcrette, J.-J., Rayner, N. A., Saunders, R. W., Simon, P., Sterl, A.,
564 Trenberth, K. E., Untch, A., Vasiljevic, D., Viterbo, P., and Woollen, J.: The ERA-40 re-analysis,
565 *Quarterly Journal of the Royal Meteorological Society*, 131, 2961–3012, doi:10.1256/qj.04.176,
566 2005.
- 567 Walsh, J. E.: Intensified warming of the Arctic: Causes and impacts on middle Latitudes, *Glob. Planet.*
568 *Change*, 117, 52-63, doi:10.1016/j.gloplacha.2014.03.003 , 2014.
- 569 Vihma, T.: Effects of Arctic sea ice decline on weather and climate: A review, *Surv. Geophys.*, 35,
570 1175-1214, doi:10.1007/s10712-014-9284-0 , 2014.
- 571 Vihma, T., Graverson, R., Chen, L., Handorf, D., Skific, N., Francis, J. A., Tyrrell, N., Hall, R., Hanna,
572 E., Uotila, P., Dethloff, K., Karpechko, A. Y., Björnsson, H., and Overland, J. E.: Effects of the
573 tropospheric large-scale circulation on European winter temperatures during the period of amplified
574 Arctic warming, *Int. J. Climatol.*, doi:10.1002/joc.6225, 2019.
- 575 Yoo, C., Feldstein, S., and Lee, S.: The impact of the Madden–Julian oscillation trend on the Arctic
576 amplification of surface air temperature during the 1979–2008 boreal winter, *Geophys. Res.*



577 Lett., 38, L24804, doi:10.1029/2011GL049881, 2011.

578 Yu, L., Zhong, S., Winkler, J. A., Zhou, M., Lenschow, D. H., Li, B., Wang, X., and Yang, Q.: Possible

579 connections of the opposite trends in Arctic and Antarctic sea-ice cover, Scientific Reports, 7,

580 45804, doi:10.1038/srep45804, 2017.

581

582

583



584 Table 1. Spatial correlations (Corrs) between the daily winter (DJF) surface air
585 temperature and the corresponding SOM pattern for each day from 1979 to 2018.

	3×1	2×2	3×2	4×2	3×3	5×2	4×3	5×3	4×4
Corr	0.26	0.43	0.48	0.48	0.50	0.49	0.50	0.51	0.51

586

587

588

589

590

591

592

593

594

595

596

597

598

599

600

601

602

603

604

605

606

607

608

609

610

611

612

613

614

615



616 Table 2. Averaged anomalous NAO and AO indices for all occurrences of each SOM
617 node. Asterisks indicate the above 95% confidence level.

618

	Node1	Node2	Node3	Node4	Node5	Node6	Node7	Node8	Node9
NAO	0.38*	0.22*	0.12*	0.05	-0.22*	-0.02	-0.07	-0.31*	-0.32*
AO	0.44*	0.38*	1.03*	-0.42	-0.62*	0.22*	-0.44*	-1.11*	-0.41*

619
620
621
622
623
624
625
626
627
628
629
630
631
632
633
634
635
636
637
638
639
640
641
642
643
644
645
646
647
648
649
650
651
652
653
654
655
656



657 Table 3. Trends in the frequency of occurrences for each SOM node (day yr^{-1}).
658 Asterisks indicate the above 95% confidence level.
659

	Node1	Node2	Node3	Node4	Node5	Node6	Node7	Node8	Node9
Trend	0.80*	0.10	-0.18	0.22*	-0.02	-0.39*	0.17	-0.17	-0.50*

660
661
662
663
664
665
666
667
668
669
670
671
672
673
674
675
676
677
678
679
680
681
682
683
684
685
686
687
688
689
690
691
692
693
694
695
696



697 Table 4. Frequencies of occurrence (%) of wintertime surface air temperature patterns
698 in Figure 1 for all winters before 1998 and after 1998 for the period 1979-2019.
699 Values with Asterisks are significantly different from climatology above the 95%
700 confidence level.
701

SOM patterns	Frequencies of occurrence		
	All winters	Winters before 1998	Winters after 1998
Node 1	17.1	7.4*	26.8
Node 2	4.4	3.3	5.4
Node 3	17.2	18.8	15.6
Node 4	8.6	5.4	11.7
Node 5	3.4	3.4	3.5
Node 6	10.2	15.2*	2.1*
Node 7	13.7	10.6	16.8
Node 8	10.1	12.1	8.0
Node 9	15.4	23.7*	7.1*

702
703
704
705
706
707
708
709
710
711
712
713
714
715
716
717
718
719
720
721
722
723
724
725
726
727
728



729 **Figure Captions**

730 Figure 1. Spatial patterns of SOM nodes for daily wintertime (December, January, and
731 February) surface air temperature anomalies ($^{\circ}\text{C}$). The number in brackets denotes the
732 frequency of the occurrence for each node.

733 Figure 2. Corresponding 500-hPa geopotential height anomalies (gpm) for each SOM
734 node. Dotted regions indicate the above 95% confidence level.

735 Figure 3. The same as Figure 2, but for anomalous 850-hPa wind field (ms^{-1}).

736 Figure 4. The same as Figure 2, but for anomalous downward longwave radiation (10^5
737 W m^{-2}).

738 Figure 5. The same as Figure 2, but for anomalous turbulent heat flux (sensible and
739 latent heat) (10^5W m^{-2}). Positive values denote heat flux from atmosphere to ocean
740 and land and vice versa.

741 Figure 6. The same as Figure 2, but for anomalous sea ice concentration.

742 Figure 7. Time series of the number of days for occurrence of each SOM node in
743 Figure 1.

744 Figure 8. Total (top), SOM-explained (middle), and residual (bottom) trends in
745 wintertime surface air temperature ($^{\circ}\text{C yr}^{-1}$). Dots in the top panel indicate above 95%
746 confidence level.

747 Figure 9. Trends in surface air temperature explained by each SOM node ($^{\circ}\text{C yr}^{-1}$).
748 The percentage in the upper of each panel indicates the fraction of the total trends
749 represented by each node.

750 Figure 10. Anomalous SST ($^{\circ}\text{C}$) regressed into the normalized time series of



751 occurrence number for nodes 1, 4, 6, and 9.

752 Figure 11. As in Figure 10, but for the anomalous 500-hPa geopotential height (gpm).

753 Figure 12. The anomalous wave activity flux (vectors) and stream function (colors,
754 10^7 m²/s) regressed onto the normalized time series of occurrence number for nodes 1,
755 4, 6, and 9.

756 Figure 13. Spatial patterns of the SOM nodes for daily wintertime (December, January,
757 and February) surface air temperature anomalies (°C) for the 1851-2014 period. The
758 number in brackets denotes the frequency of the occurrence for each node.

759 Figure 14. Time series of the number of days for occurrence of each SOM node in
760 Figure 1.

761 Figure 15. The (a) leading pattern and (b) its time series (PC1 and PC2) of EOF
762 analysis of wintertime surface air temperature anomalies. Prior to EOF analysis,
763 surface air temperature data are detrended. A 40-yr low-pass filtered is applied to the
764 time series of PC1, PC2, AMO and PDO indices.

765

766

767

768

769

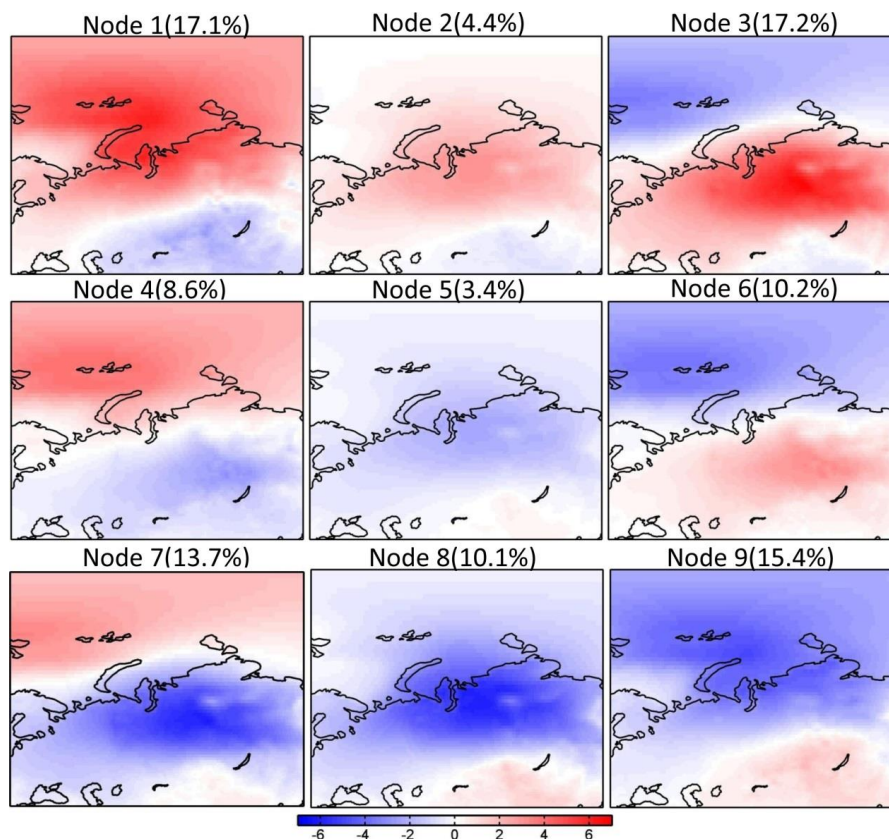
770

771

772



773



774

775 Figure 1. Spatial patterns of SOM nodes for daily wintertime (December, January, and February)
776 surface air temperature anomalies ($^{\circ}\text{C}$). The number in brackets denotes the frequency of the
777 occurrence for each node.

778

779

780

781

782

783

784

785

786

787

788

789

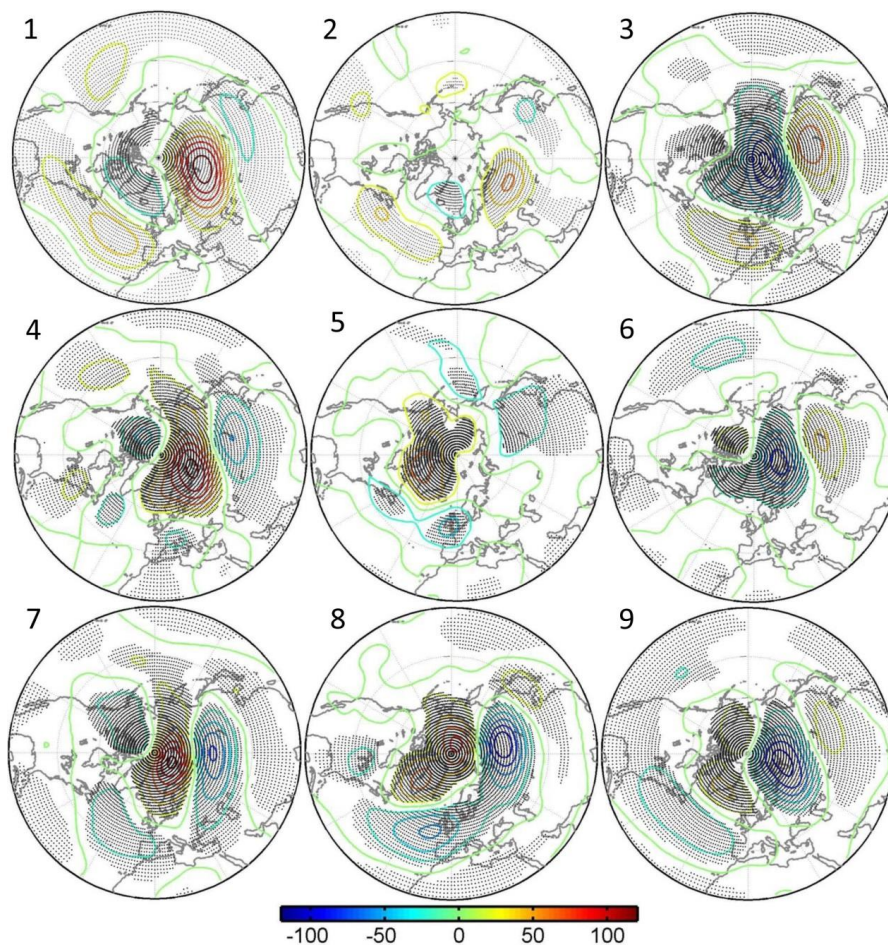
790

791

792



793



794

795 Figure 2. Corresponding 500-hPa geopotential height anomalies (gpm) for each node. Dotted
796 regions indicate the above 95% confidence level.

797

798

799

800

801

802

803

804

805

806

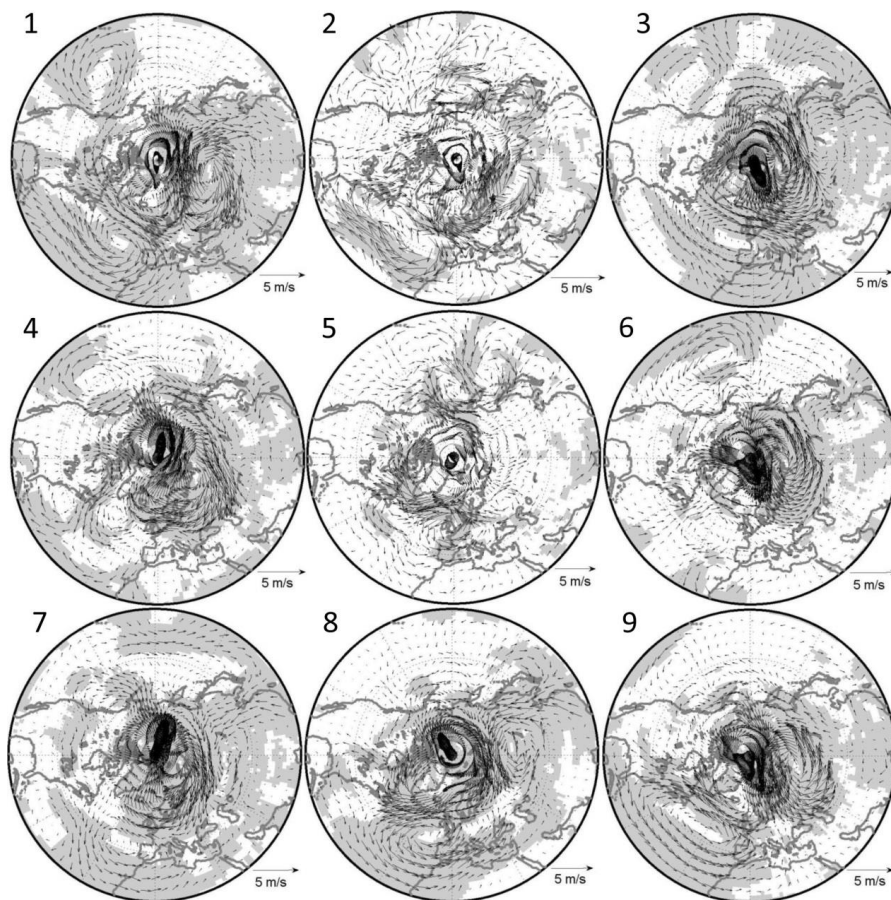
807

808

809



810



811

812 Figure 3. The same as Figure 2, but for anomalous 850-hPa wind field (ms^{-1}).

813

814

815

816

817

818

819

820

821

822

823

824

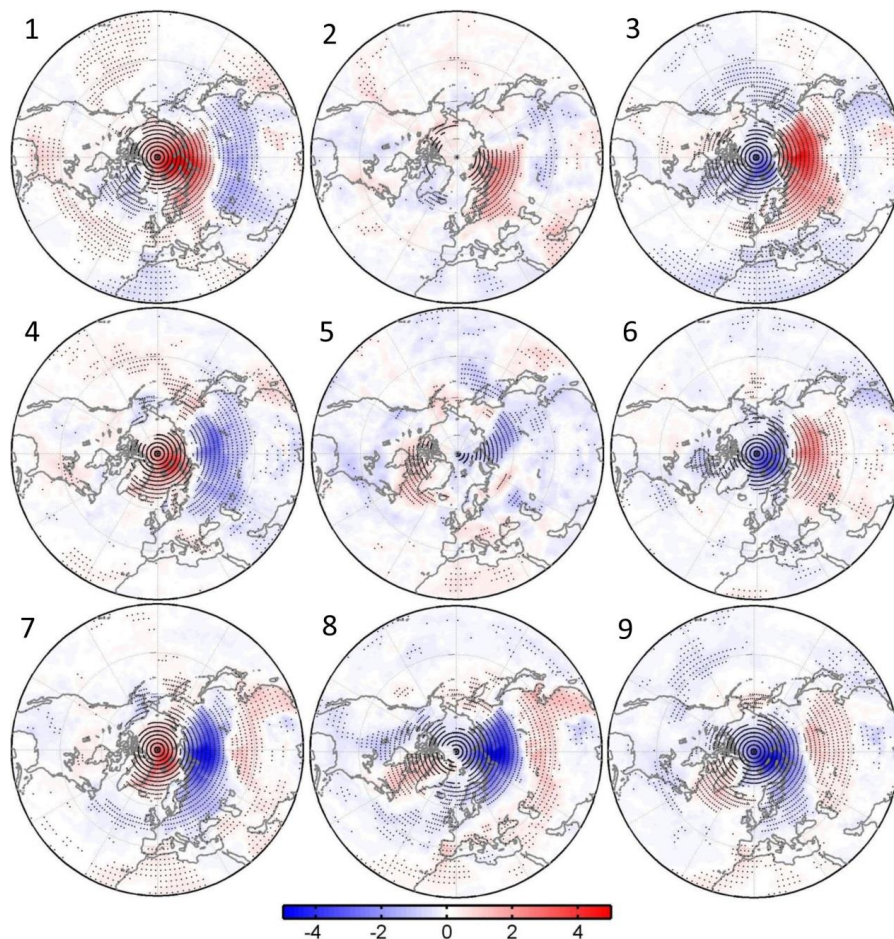
825

826

827



828



829

830 Figure 4. The same as Figure 2, but for anomalous downward longwave radiation (10^5 W m^{-2}).

831

832

833

834

835

836

837

838

839

840

841

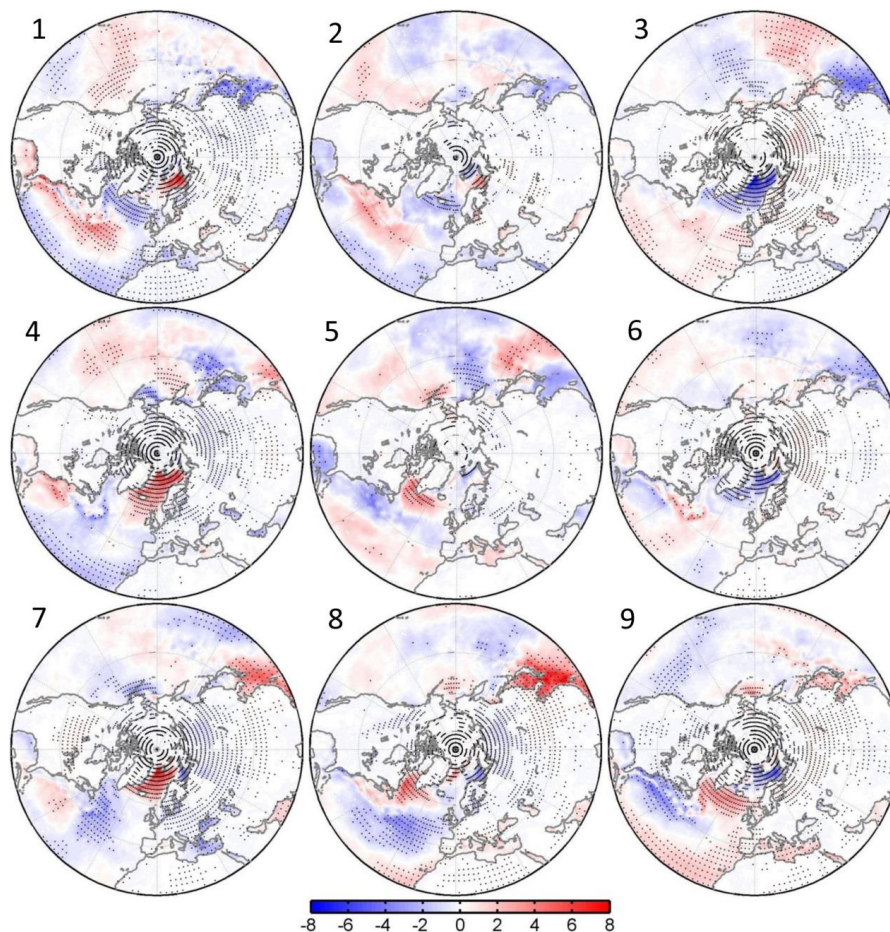
842

843

844



845



846

847 Figure 5. The same as Figure 2, but for anomalous turbulent heat flux (sensible and latent heat)
848 (10^5W m^{-2}). Positive values denote heat flux from atmosphere to ocean and vice versa.

849

850

851

852

853

854

855

856

857

858

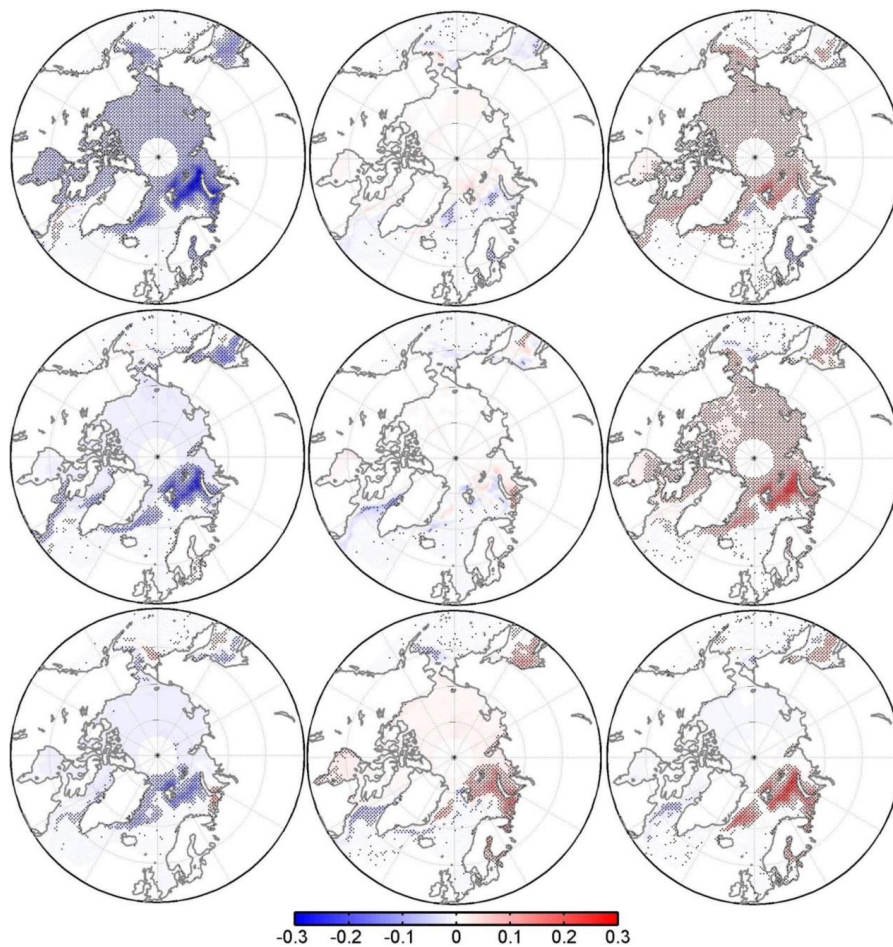
859

860

861



862



863

864

865

866

867

868

869

870

871

872

873

874

875

876

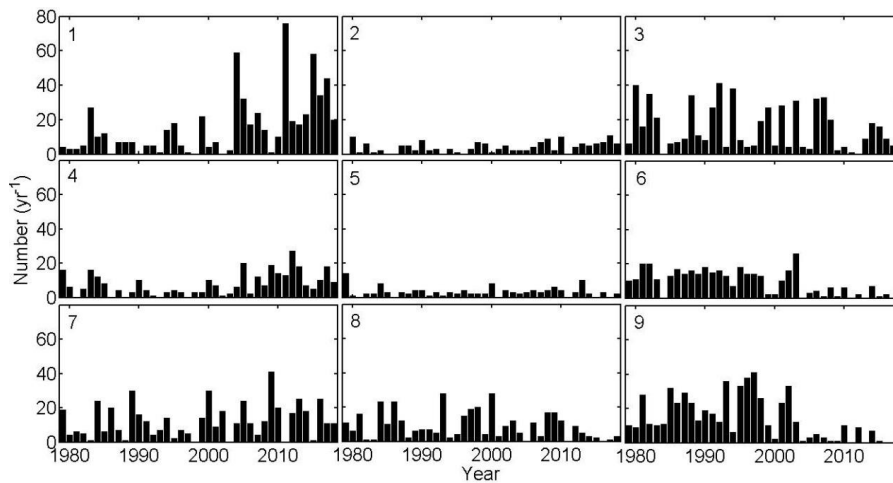
877

878

Figure 6. The same as Figure 2, but for anomalous sea ice concentration.



879



880

881 Figure 7. Time series of the number of days for occurrence of each SOM node in Figure 1.

882

883

884

885

886

887

888

889

890

891

892

893

894

895

896

897

898

899

900

901

902

903

904

905

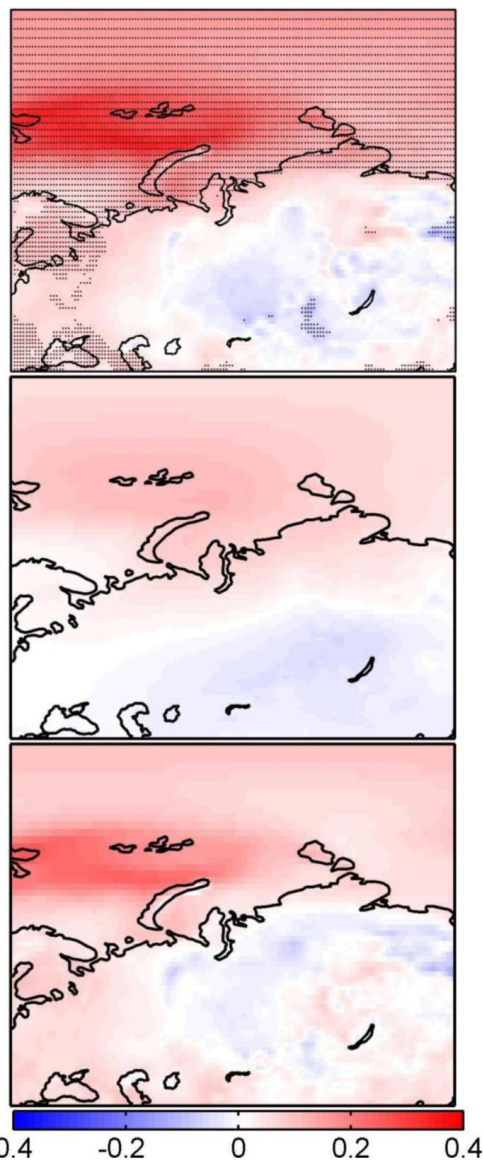
906

907

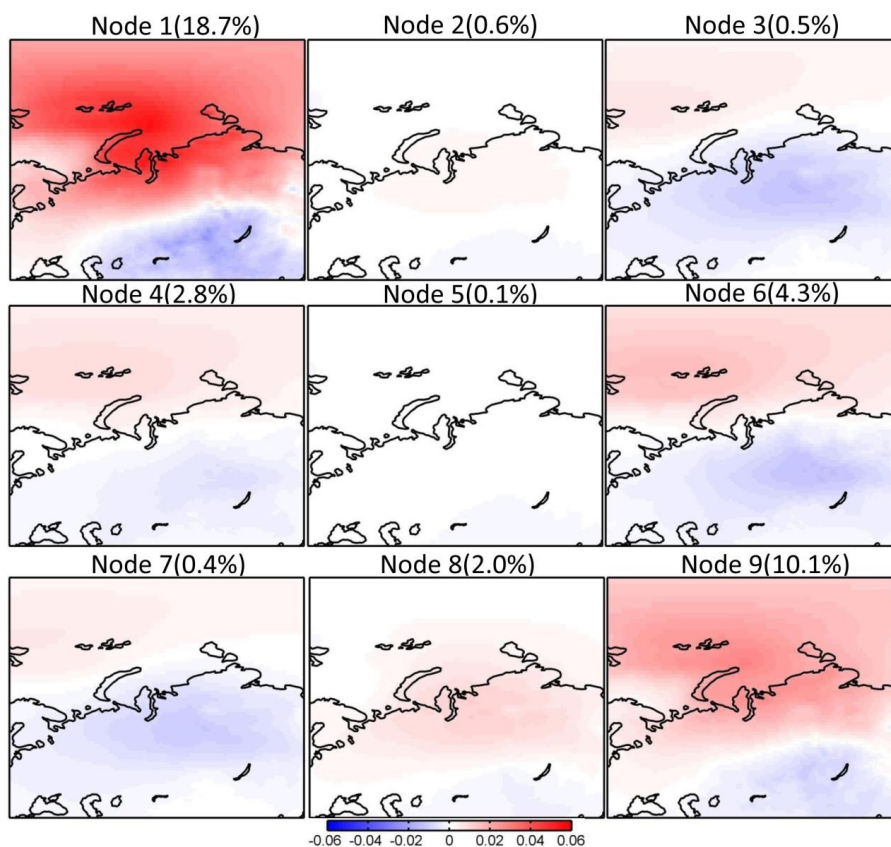
908



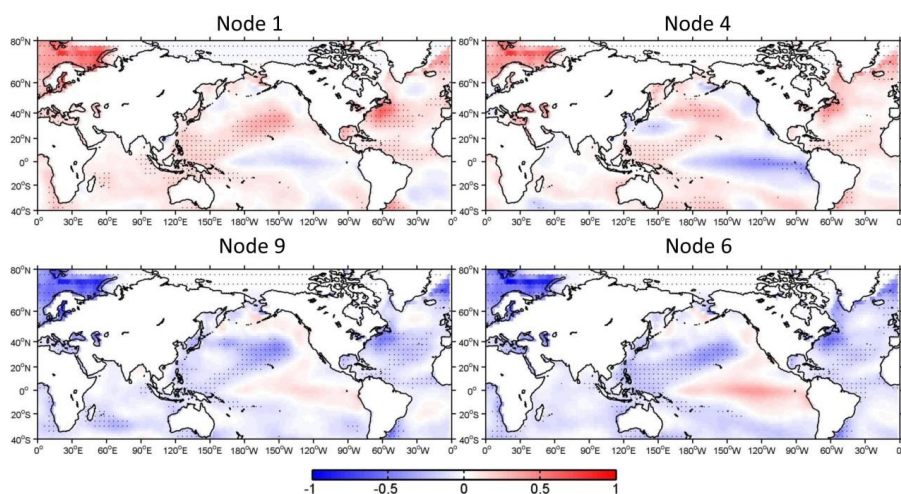
909



910 -0.4 -0.2 0 0.2 0.4
911 Figure 8. Total (top), SOM-explained (middle), and residual (bottom) trend in wintertime (DJF)
912 surface air temperature ($^{\circ}\text{C yr}^{-1}$). Dots in the top panel indicate above 95% confidence level.
913



914
915 Figure 9. Trends in surface air temperature explained by each SOM node ($^{\circ}\text{C yr}^{-1}$). The percentage
916 in the upper of each panel indicates the fraction of the total trend represented by each node.
917
918
919
920
921
922
923
924
925
926
927
928
929
930
931
932
933



934

935 Figure 10. Anomalous SST ($^{\circ}\text{C}$) regressed into the normalized time series of occurrence number
936 for nodes 1, 4, 6, and 9.

937

938

939

940

941

942

943

944

945

946

947

948

949

950

951

952

953

954

955

956

957

958

959

960

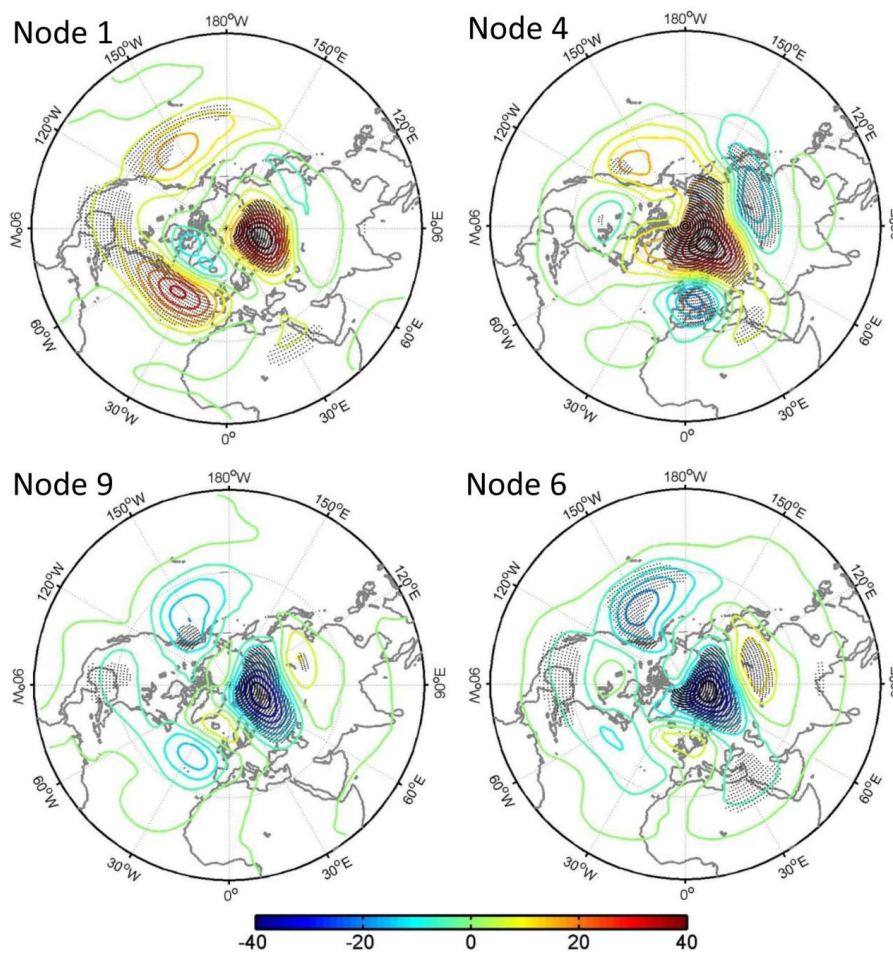
961

962

963



964



965

966 Figure 11. As in Fig. 10, but for the anomalous 500-hPa geopotential height (gpm).

967

968

969

970

971

972

973

974

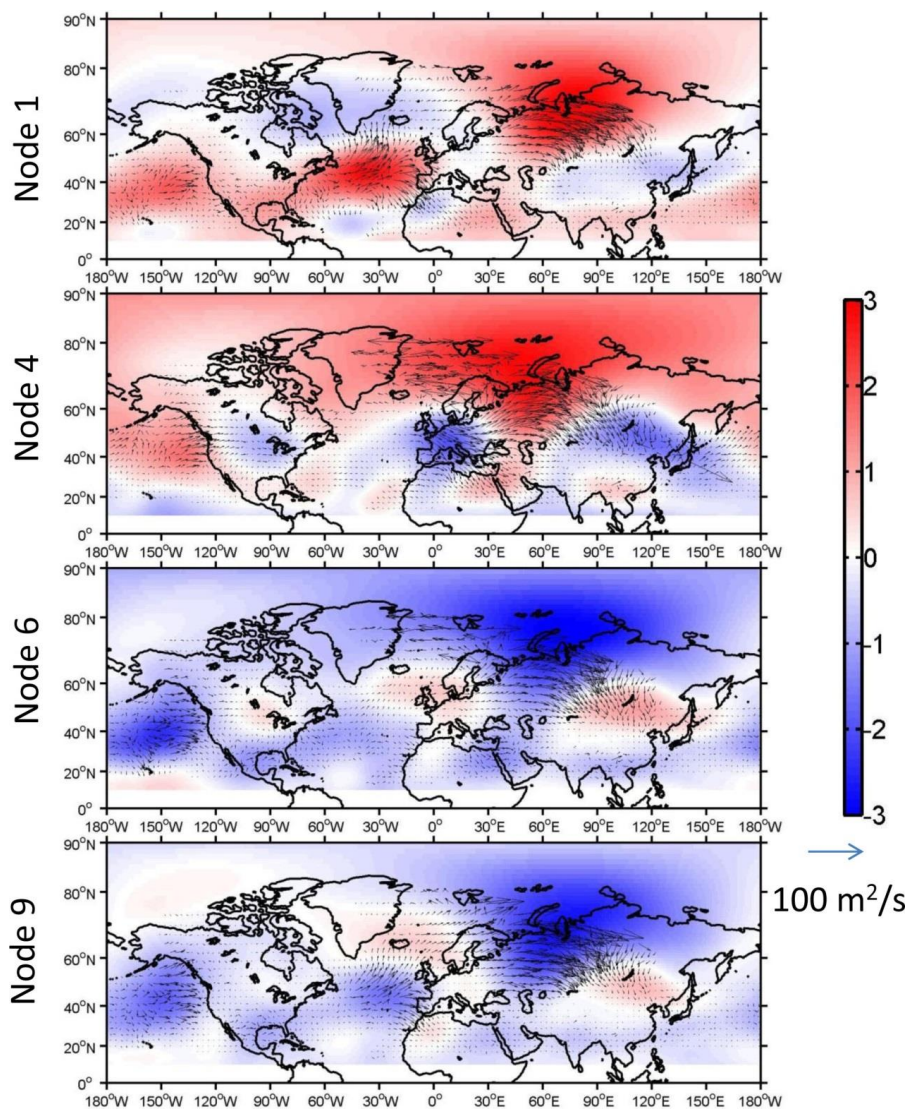
975

976

977

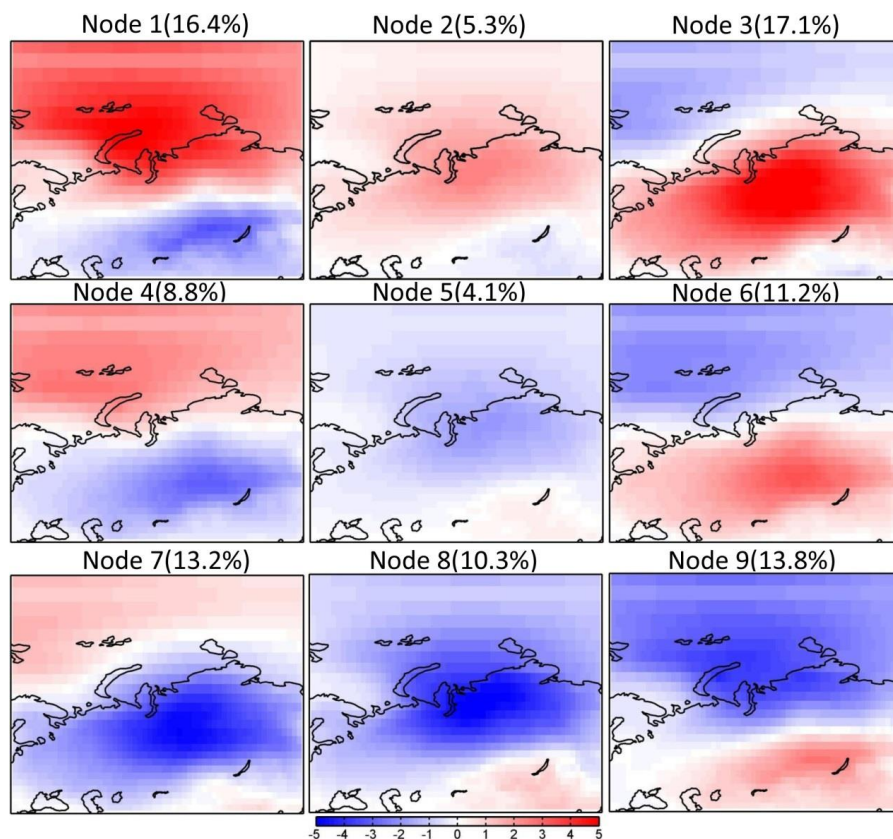
978

979



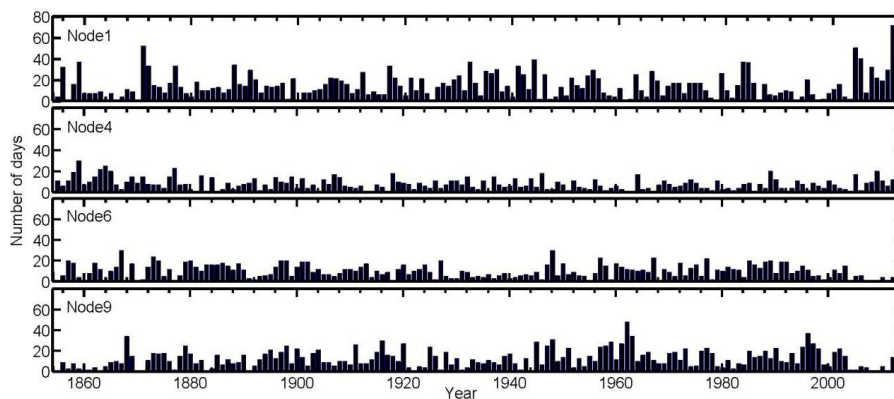
980
981 Figure 12. The anomalous wave activity flux (vectors) and stream function (colors, units: $10^7 \text{ m}^2/\text{s}$)
982 regressed onto the normalized time series of occurrence number for nodes 1, 4, 6, and 9.
983

984
985
986
987
988
989
990
991



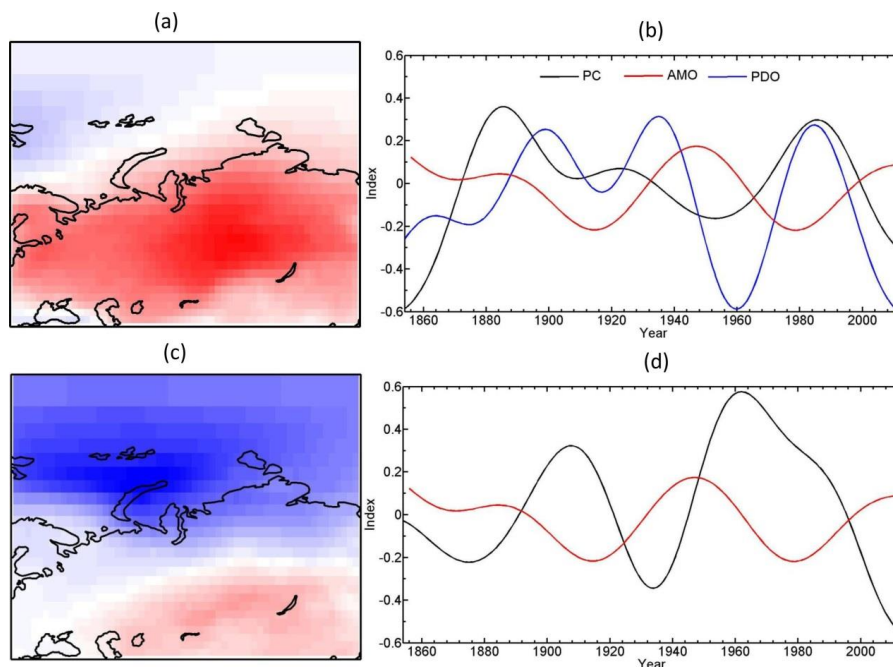
992
993 Figure 13. Spatial patterns of SOM nodes for daily wintertime (December, January, and February)
994 surface air temperature anomalies ($^{\circ}\text{C}$) for the 1851-2014. The number in brackets denotes the
995 frequency of the occurrence for each node.
996
997
998
999

1000
1001
1002
1003
1004
1005
1006
1007
1008
1009
1010
1011



1012
1013
1014
1015
1016
1017
1018
1019
1020
1021
1022
1023
1024
1025
1026
1027
1028
1029
1030
1031
1032
1033
1034
1035
1036
1037
1038
1039
1040
1041
1042
1043
1044

Figure 14. Time series of the number of days for occurrence of each SOM node in Figure 13.



1045

1046 Figure 15. The (a) leading pattern and (b) its time series (PC1 and PC2) of EOF analysis of
1047 wintertime surface air temperature anomalies. Prior to EOF analysis, surface air temperature data
1048 are detrended. A 40-yr low-pass filter is applied to the time series of PC1, PC2, AMO and PDO
1049 indices.

1050